Effect of two-dimensional surface irregularities on swept wing transition
Forward facing steps

Rius Vidales, Alberto F.; Kotsonis, Marios; Antunes, Alexandre; Cosin, Renato

DOI
10.2514/6.2018-3075

Publication date
2018

Document Version
Accepted author manuscript

Published in
2018 Fluid Dynamics Conference

Effect of Two-Dimensional Surface Irregularities on Swept Wing Transition: Forward Facing Steps

Alberto F. Rius Vidales* and Marios Kotsonis†
Delft University of Technology, Delft, The Netherlands, 2629HS

Alexandre Antunes‡ and Renato Cosin§
Embraer S.A., São José dos Campos, Brazil, 12227-901

An experimental investigation was carried out to examine the effect of two-dimensional Forward Facing Steps surface irregularities, on the laminar-to-turbulent boundary-layer transition on a 45° swept-wing. For the clean reference case, the numerical boundary-layer flow is calculated from pressure measurements, and a thorough linear stability analysis is performed for all variations of Reynolds number and angle of attack. Infrared thermography is employed to determine the transition-front location which is associated to an N-Factor, calculated from the linear stability analysis. The change in the amplification factor ΔN, caused by the addition of the surface irregularity, is analyzed. The reduction in the critical N-factor is observed to correlate with the estimated cross-flow instability vortex core height to step height ratio and the relative step height. The work presented in this paper is part of an ongoing research project to characterize the effect that surface irregularities have on boundary layer transition. The ΔN-method offers an overview of the phenomena related to FFS, capable of guiding future investigations into the underlying flow mechanisms.

Nomenclature

c	=	Chord dimension, m.
b	=	Wing span dimension, m.
AR	=	Wing aspect ratio.
S	=	Wing planform area, m^2.
Λ	=	Sweep angle, deg.
λ_T	=	Wing taper ratio
U_∞	=	Free-stream velocity, $m\,s^{-1}$.
α	=	Angle of attack, deg.
Re_{c_X}	=	Reynolds number ($U_\infty c_X/\nu$).
h_2	=	Forward facing step height, μm.
h_c	=	Critical step height, μm.
x_h	=	Surface irregularity location, m.
δ^*	=	Boundary-layer displacement thickness, m.
x_t	=	Transition location, m.
X, Y, Z	=	Reference coordinate system parallel to the wind tunnel floor.
x, y, z	=	Reference coordinate system orthogonal to the leading edge.
R_q	=	Root mean square surface roughness, μm.
y_c	=	Estimated cross-flow instability vortex core height, mm.

*PhD Candidate, Section of Aerodynamics, Faculty of Aerospace Engineering, AIAA Student Member
†Assistant Professor, Section of Aerodynamics, Faculty of Aerospace Engineering
‡Product Development Engineer, Aerodynamics and CFD R&D Department.
§Product Development Engineer, Aerodynamics and CFD R&D Department.
. * Email address for correspondence: a.f.riusvidales@tudelft.nl

I. Introduction

At the beginning of the 20th century, the benefits of air transportation were only available to a handful of travelers. Nowadays, it is an ordinary method of transportation, which 3.8 billion travelers used in 2016. According to the International Air Transport Association (IATA) [1], it is likely that the number of passengers will increase to 7.2 billion by 2035. The continuous development of this market motivates aircraft manufacturers to constantly optimize their products to reduce fuel consumption, thus offering airlines the opportunity to reduce their environmental impact. This is important since the carbon dioxide emissions are expected to increase in over a 110 percent for the international aviation sector during the period 2005 to 2025 [2].

When considering the aerodynamic performance, the idea of reducing skin-friction drag is very attractive, since it is known to account for almost half of the total drag of a subsonic transport aircraft [3]. Until now several active and passive flow control techniques have been developed to stabilize the boundary-layer flow and delay laminar-to-turbulent transition over the external surface of the aircraft. Nevertheless, the effectiveness of these techniques is hindered by particular constraints in current aircraft design, construction, and maintenance. Especially relevant to laminar flow is the existence of non-smooth surfaces where two-dimensional irregularities in the form of steps and gaps are present. These irregularities are typically due to structural and manufacturing reasons since the aircraft skin is integrated by several panels commonly joined using a lap-splice or a single strap arrangement [4], as illustrated in Fig. 1.

The study of the effect of these two-dimensional surface irregularities on boundary-layer transition is of paramount importance for the implementation of active and passive flow control techniques in the aviation industry. Previous studies have mainly focused on unswept flat-plates [5–7] and wing models [8–10] where Tollmien-Schlichting (TS) waves instability is dominant. Due to the limited applicability of these results to swept wings found in almost every contemporary transport aircraft, recent studies [11–18] were conducted in three-dimensional boundary-layers, where cross-flow (CFI) instability is present.

When considering surface irregularities in the form of steps, it has been widely noted [5, 11, 14] that setting the step in a forward facing manner, results in a milder detrimental effect on boundary layer transition than that resulting from a backward-facing arrangement. This general consensus applies irrespective of whether the laminar-to-turbulent boundary layer transition is dominated by TS-waves or CFI. Therefore, it has become a common practice in the design of laminar flow components to set unavoidable surface irregularities to resemble a FFS geometry in order to increase the manufacturing tolerances. The present research contributes to the body of knowledge by analyzing the effects that this type of surface irregularities have on the stability of the boundary-layer flow in a swept-wing model. The results presented here are part of the Laminar Flow Technology Research Project currently conducted by Delft University of Technology in collaboration with Embraer S.A. R&D Department.

The structure of this paper is the following: Sec. II provides a detailed description of the, swept-wing model, the aerodynamic add-ons designed to produce two-dimensional irregularities on its surface and a description of the wind tunnel facility, measurement technique, and procedure to identify the transition front. In Sec. III, the stability calculations, and methodology followed in the analysis of the boundary layer flow development are described; and Sec. IV presents a discussion of the results.

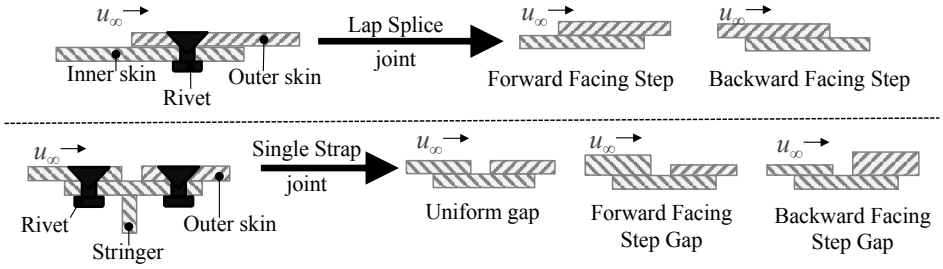

Fig. 1 Diagram of surface irregularities on aircraft skin panels; Left: Schematics of commonly used surface panel joints, Right: Conceptualised types of surface irregularities resulting from panel joints.

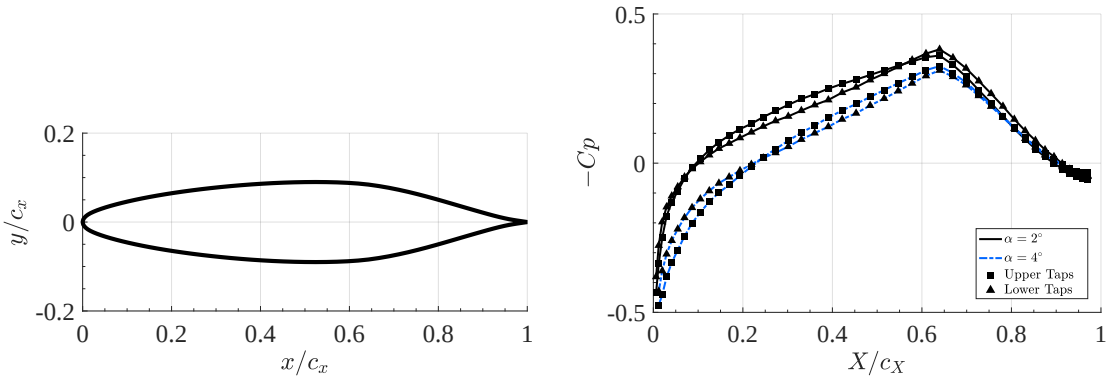

Fig. 2 M3J airfoil geometry (a), orthogonal to the leading edge and Swept-Wing M3J pressure distribution (b), measured by the upper ($Z = 0.75b$) and lower ($Z = 0.25b$) arrays of pressure taps at $\alpha = 2°$ and $4°$ (measurement on the pressure side of the wing) at $Re_{c_X} = 4.89 \times 10^6$.

II. Experimental Setup

This section provides an overview of the swept-wing model, the surface add-ons designed to produce two-dimensional irregularities, and a description of the wind tunnel facility, measurement technique, and procedure to identify the transition front.

A. Swept-Wing Model

The wind tunnel model used, is an in-house designed [19] swept-wing, known as the M3J. This model has been extensively used at TU Delft for the detailed study of the primary and secondary cross-flow instability [20] and boundary layer control [21, 22]. The geometric parameters of the model are summarized in Table. 1. The wing features a modified NACA 6-series (66018) airfoil, as illustrated in Fig. 2(a). At mild angles of attack, the stream-wise pressure distribution on the pressure side of the wing (Fig. 2(b)) shows a favorable pressure gradient up until $X/c_X \approx 0.65$; avoiding the amplification of Tollmien-Schlichting waves instability. Moreover, a small leading edge radius and the lack of concave surfaces leads to the suppression of attachment line and Görtler instabilities, respectively. Therefore, for this model, cross-flow is the dominant instability in the laminar-to-turbulent boundary-layer transition process [20].

As illustrated in Fig. 3(a), the model pressure distribution is measured along the stream-wise direction (X) at two different span-wise locations, namely at 25% and 75% of the model span (b). At each of the aforementioned locations, 46 stream-wise oriented pressure taps record the model pressure distribution. From these measurements, the external inviscid velocity is calculated and used to numerically solve for the boundary-layer flow on the pressure side of the model.

The M3J aerodynamic design, allows infinite swept-wing conditions at the measurement region in order to study fundamental features of cross-flow dominated transition [19]. Although wall-liners were initially designed and manufactured for this model, previous experimental results suggest that the aspect ratio (AR) is sufficient to achieve span-wise invariant conditions [20]. Figure. 2(b) shows both upper and lower pressure distribution for two angles of attack (α). The small variation between the upper and lower pressure measurements indicate that the infinite swept-wing condition is a valid assumption at mild angles of attack.

Finally, it is important to note that throughout this study two different coordinate systems are used. The first one, is aligned with the wind tunnel floor where the spatial components are given by X, Y, Z and the velocity components by U, V, W. The second coordinate system is aligned to the leading edge with x, y, z and u, v, w as illustrated in Fig. 3(a).

Table 1 Geometric parameters of M3J swept-wing model.

Parameter	Λ	AR	b	c_X	c_x	λ_T	S	R_q
Value	45°	1.01	1.25 m	1.27 m	0.9 m	1.00	1.58 m^2	0.20 µm

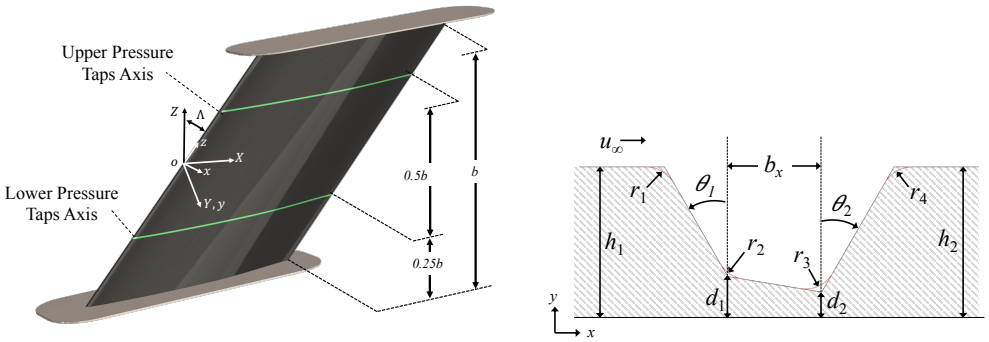

(a) (b)

Fig. 3 Schematics of wind tunnel model and surface irregularities; (a) M3J swept-wing model diagram, indicating the coordinate systems, un-swept (X, Y, Z) and swept (x, y, z), and the location of the upper and lower row of pressure taps. (b) Local geometric parameters concerning two dimensional surface irregularities.

B. Two-Dimensional Surface Irregularities Add-ons

Wind tunnel surface irregularity add-ons were designed and manufactured to conduct an extensive parametric study. Similarly as in [8, 11], foils are used to create surface irregularities. For this study, Polyethylene Terephthalate (PET) foils of different thickness were cut using a CNC DCS 2500 Gerber machine. As illustrated in Fig. 4, through the combination of different foils it is possible to create the three main types of two-dimensional surface irregularities: forward facing steps (FFS), backward facing steps (BFS) and uniform gaps (G-UNF). Figure. 3(b) presents the main local geometrical parameters concerning the surface irregularity. In this work only sharp ($r_{1-4} = 0$ mm), straight ($\theta_{1,2} = 0°$) FFS ($h_1 = 0$ mm, $b_x = d_{1,2} = 0$ mm and $h_2 > 0$ mm) geometries are presented.

Table 2 Local geometrical parameters of tested cases.

ID	$\bar{h_2}$ [µm]	σ_{h_2} [µm]	R_q[µm]	x_{h_2}/c_x
Clean-ST	-	-	0.20	-
Clean-TR	-	-	0.02	-
FFS-A	549	7.5	0.045	0.2
FFS-B	734	4.2	0.02	0.2
FFS-C	951	16.5	0.02	0.2

The FFS step height was measured with the foil installed on the model for every tested case. The measurements were performed by traversing a Micro-Epsilon 2950-25 laser line scanner (reference resolution $y_L = 2$ µm) along the span-wise extent of the surface irregularity. Due to the extreme sensitivity of CFI to surface roughness, great care was taken to ensure a consistent and polished foil surface, especially near the leading edge region. The foil roughness was monitored using a Mitutoyo SJ-310 tester. Table. 2 summarizes, the resulting average step height ($\bar{h_2}$), standard deviation (σ_{h_2}), surface roughness (R_q) and stream-wise location (x_{h_2}/c_x) of the different configurations. Finally, it is important to note that the Clean-TR case, presented in Fig. 4(a), features a foil which extends until the model trailing edge.

(a) (b) (c) (d)

Fig. 4 Schematic of two-dimensional surface irregularities installed on the M3J model; (a) Clean-TR. (b) Backward facing step BFS. (c) Forward facing step FFS. (d) Gap

C. Wind Tunnel Facility

The measurements were conducted at the Low Turbulence Tunnel (LTT) of the Delft University of Technology. This facility is an atmospheric closed return tunnel which features a contraction ratio of 17:1 and an octagonal test-section with a height of 1.25 m, a width of 1.80 m, and length of 2.6 m. As part of the flow characterization of this facility [23], measurements upstream of the test-section with the M3J model installed, were performed using a hot-wire sensor. For the condition when seven anti-turbulence screens are active, the results are shown in Fig. 5. After applying a bandpass filter in the range $2Hz$ to $5kHz$, the turbulence intensity $Tu/U_\infty \leq 0.04\%$ for the free-stream velocity range $25\ \mathrm{m\,s^{-1}} \leq U_\infty \leq 75\ \mathrm{m\,s^{-1}}$ under which the tunnel was operated during this study. The work presented in [20] show that this combination of wind tunnel facility and model offers the possibility to study laminar-to-turbulent boundary layer transition caused by stationary cross-flow instability.

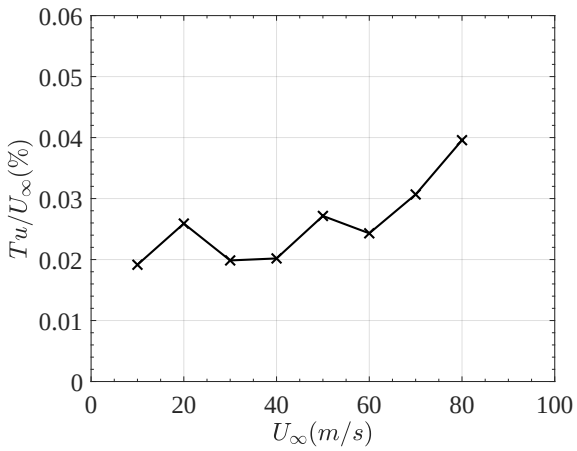

Fig. 5 Low Turbulence Tunnel (LTT) measured turbulence intensity with M3J model installed in the test-section.

D. Infrared Thermography

The distinct heat transfer properties between a laminar and a turbulent boundary-layer allows determining the location of laminar-to-turbulent boundary layer transition by measuring the model surface temperature using an infrared thermographic system (IR). The non-intrusiveness, flexibility, and simplicity offered by this measurement technique, results in an ideal transition identification method for large parametric studies, such as the one presented here.

Measurements were performed, on the pressure side of the wing, for a range of Reynolds number between

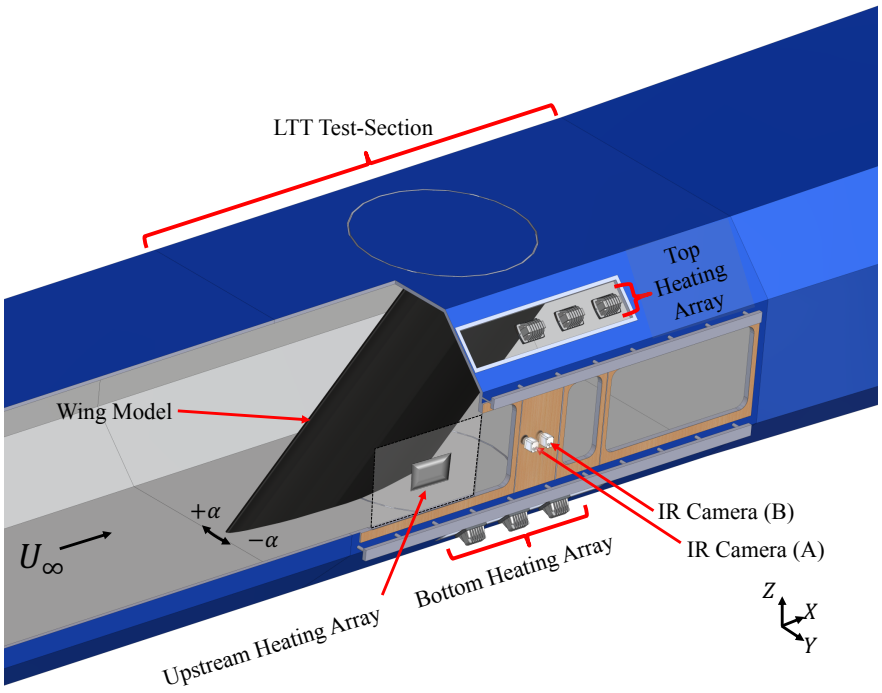

Fig. 6 Schematic of the infrared thermography setup (flow direction is from left to right). Two IR cameras are located outside the test-section. The model is illuminated from the exterior of the test-section by three heating arrays. Note that the test-section features a cut-out only present in this drawing for better visualization.

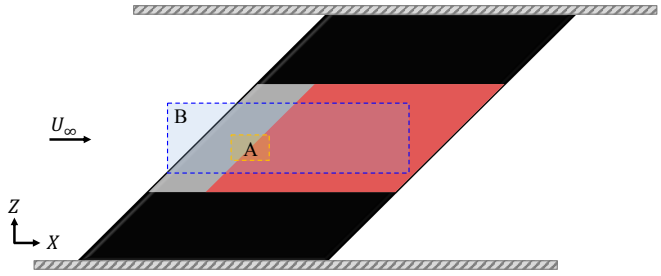

Fig. 7 Schematic of IR imaging, showing a side view of the M3J model indicating the locaiton of the final analysis region for camera (A) and camera (B).

$2.1 \times 10^6 \leq Re_{c_X} \leq 6.1 \times 10^6$ based on the free-stream velocity (U_∞) and the stream-wise chord length (c_X). For each Re_{c_x} condition, the angle of attack (α) was gradually varied from 1.35° to 5.35°.

A diagram of the complete experimental setup installed on the LTT wind tunnel test-section is presented in Fig. 6. In order to increase the thermal contrast on the IR images, the model was irradiated by a total of seven halogen lamps. Six lamps of 400 W were located at the optical access ports on the upper and lower parts of the test-section and one of 1000 W was located at mid-test section height upstream of the IR cameras.

Two Optris PI640 IR cameras, featuring a 640px × 480px un-cooled focal plane array (FPA) sensor with a thermal sensitivity (NETD) of 75 mK, image the pressure side of the model through small openings on the vertical wall of the test-section. The upstream camera (A) used for close inspection during the tests was equipped with a zoom lens $f = 41.5$ mm, in order to image a region in the vicinity of the step. The downstream camera (B) was equipped with a wide angle lens, $f = 10.5$ mm, imaging a larger portion of the model.

The IR image processing and transition location extraction were performed using an in-house semiautomated technique. To account for the airfoil curvature and image deformation inherent to the fixed position of the camera, a calibration was performed by imaging a target fixed on the model surface at every angle of attack condition. Later using this spatial relation a dewarping of the IR images was performed. For the downstream camera (B), used to determine the transition location, the analysis region dimensions are 1037 mm × 240 mm centered at $X/c_X = 0.44$ and $Z/b = 0.03$, as delimited by dashed blue lines in Fig. 7. For every combination of free-stream velocity and angle of attack this camera acquired 38 images at 5 Hz. In order to increase the signal to noise ratio, from each measurement series a time averaged is calculated. In order to decrease the possibility of a spurious identification of the transition front a differential infrared thermography (DIT) approach, similar as the one presented by [24, 25], is applied on consecutive IR Images with increasing Reynolds number for a fixed angle of attack. To illustrate the method, consider the time averaged IR images $\bar{I}_A$ ($\alpha = 2.9°, Re_{c_X} = 2.75 \times 10^6$) and $\bar{I}_B$ ($\alpha = 2.9°, Re_{c_X} = 2.97 \times 10^6$). Then using Eq. 1 the DIT is calculated. As illustrated in Fig.8, the IR image $\bar{I}_{DIT}$ contains information of the transition location for both conditions $\bar{I}_A$ and $\bar{I}_B$.

$$\bar{I}_A - \bar{I}_B = \bar{I}_{DIT} \tag{1}$$

In this semiautomated transition identification routine, a new method is proposed. This method use a computer vision technique known as connected components labeling analysis[26] to estimate apriori the transition location. With this information it is possible to adjust the downstream limit of the analysis region dynamically. Initially, each IR image $\bar{I}_{DIT}$ is binarized using the thresholding method proposed in [27], later regions of connected pixels are calculated based on the method described in [26]. The region with the maximum area is considered to correspond to the laminar fraction between $\bar{I}_A$ and $\bar{I}_B$, so the projection of its centroid to the mid-span axis ($Y/b = 0$) is used to determine the downstream limit of the analysis region, as indicated in Fig. 8. On the other hand, the upstream limit remains fixed, such that all the conditions where the transition occurs upstream of this limit are discarded from the analysis.

From Reynolds analogy, it is known that an increase in wall shear-stress resulting from a turbulent boundary-layer leads to an increase in the surface heat transfer, which in turn leads to a lower surface temperature when compared to the regions where the flow is laminar. Hence, the transition location is identified by calculating the temperature gradient of the entire image. To increase the robustness of the identification, outliers are removed based on the standard deviation of the detected positions. Finally, a linear fit of the transition front is calculated for the entire span. Moreover, the confidence bands of the fit indicate the uniformity of the front.

An essential aspect of a semiautomated transition identification routine is to be able to detect when the flow in the analysis region is fully turbulent. To avoid a false identification, a knowledge-based approach is conducted individually

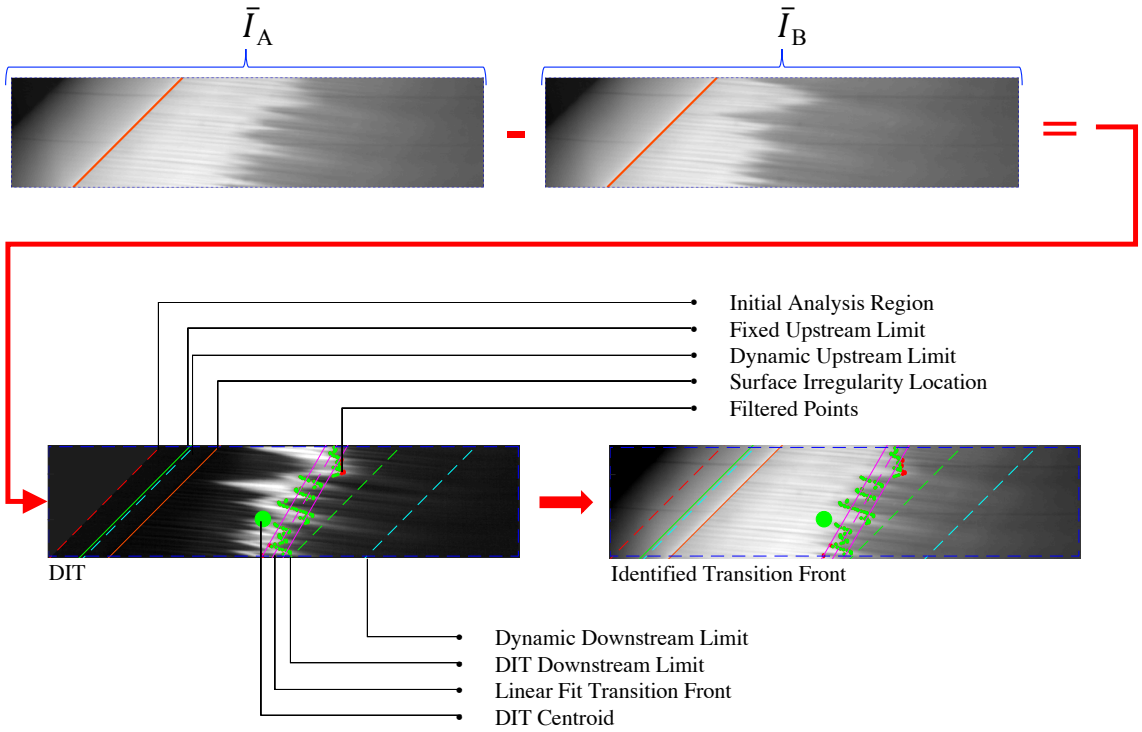

Fig. 8 Schematic of transition location identification (flow direction is from left to right) for configuration FFS-B at $\alpha = 2.9°$ and $Re_{c_X} = 2.75 \times 10^6$, showing the IR source images $\bar{I}_A$ ($Re_{c_X} = 2.75 \times 10^6$) and $\bar{I}_B$ ($Re_{c_X} = 2.97 \times 10^6$), in conjunction with the main parameters of the analysis.

for each angle of attack case. For instance, consider the case when $\alpha = 2.9°$. The lowest Re_{c_X} condition is visually inspected, and the user determines, whether the analysis region is fully turbulent or not. Based on this first inspection, the algorithm will continue to analyze higher Re_{c_X} conditions where the transition location is expected to occur upstream or in the vicinity of the previous location. A comparison of DIT centroid with the previously identified transition location is performed. If the DIT centroid is downstream, then it is considered that the flow has become fully turbulent since it was assumed that an increase in Re_{c_X} should no result in a delay of the transition location. It is important to highlight that, the results presented in the following sections discard the cases considered to be fully turbulent or spurious in the analysis region to avoid conclusions that could be based on a false identification of the transition location.

III. Methodology

This section describes the methodology followed in the analysis of the transition development resulting from the addition of a two dimensional irregularity in the form of a FFS step on the M3J swept-wing model surface. The IR images are processed and the transition front extracted for each experimental condition, following the procedure presented in Sec. II.D,

To illustrate the methodology followed during the analysis of the results, consider the condition $\alpha = 2.9°$ at $Re_{c_X} = 2.95 \times 10^6$. For the Clean-TR case, where no irregularities are present on the model surface, laminar-to-turbulent boundary layer transition occurs at a chord-wise location of $x_{t,C}/c_x = 0.43$.

As illustrated in Fig. 9(a), a characteristic jagged pattern of turbulent wedges is observed for this condition, suggesting that stationary cross-flow is responsible for the laminar breakdown of the boundary-layer flow. The addition of a forward facing step FFS-C ($\bar{h}_2 = 951$ µm at $x_{h_2}/c_x = 0.2$) results in a similar transition pattern while displaying a decrease in the extent of the laminar flow region caused by an upstream movement ($x_{t,I}/c_x = 0.25$) of the transition front location, as shown in Fig. 9(b)

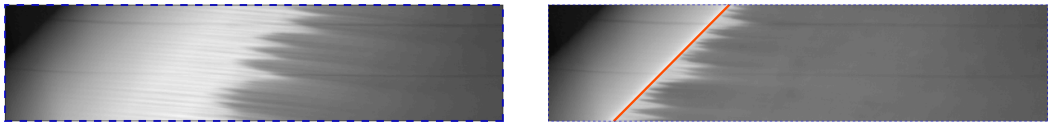

(a) (b)

Fig. 9 Infrared thermography snapshots (flow direction is from left to right) showing the effect of 2D surface imperfection on the transition location at $\alpha = 2.9°$, $Re_{c_X} = 2.95 \times 10^6$, the dashed blue line denotes the initial analysis region, the orange line indicates the step location; (a) Clean-TR, only the base-foil is installed, no surface irregularity (b) FFS-C ($\bar{h}_2 = 951\mu$m at $x_{h_2}/c_x = 0.2$)

A. Stability Analysis

Linear Stability Analysis (LST) was performed for each experimental condition using a TU-Delft in-house solver, with the objective to predict the spatial amplification of stationary CFI modes, represented by the respective N-factors. All LST calculations are based on the Clean-ST case (no surface irregularity, no base foil) measured pressure distribution. The external velocity of the boundary-layer (i.e. inviscid velocity) was calculated and used to solve for the steady, incompressible and two dimensional laminar boundary-layer flow on the pressure side of the model. A downstream marching scheme [28] along the x component (Fig. 3(a), i.e. orthogonal to the leading edge) was applied. The stability of this two-dimensional laminar boundary-layer was evaluated by considering a small wave-like disturbance given by Eq. 2.

$$\psi(x, y, z, t) = \phi(y) \exp^{i(\alpha x + \beta z - \omega t)} \tag{2}$$

The linear Orr-Sommerfeld equation (OS) was solved for the eigenfunctions $\phi(y)$, using the spatial theory formulation [29], where the angular frequency (ω) is real, and the stream-wise (α) and spanwise (β) wavenumbers are complex. The approximate span-wise invariance of the flow on the M3J model, shown in Fig. 2(b), simplifies the formulation by assuming a zero span-wise growth rate (β_i). Then, the N-factor is calculated for a combination of a given span-wise wavelength (β_r) and $\omega = 0$ (stationary) by integrating the spatial growth rate (α_i) along the x coordinate. The final result of the stability analysis is the envelope of N-curves of unstable span-wise wavelengths of all present stationary CFI modes, as illustrated by Fig. 10, for the condition $\alpha = 2.9°$ and $Re_{c_X} = 2.95 \times 10^6$ when no surface irregularity is present. The N-Factors corresponding to the transition locations for the Clean-TR ($N_C = 8.9$) and the FFS-B ($N_I = 6.8$) were determined using this envelope, as illustrated by the dashed lines in Fig. 10. Finally, the change in the N-Factor ($\Delta N = N_C - N_I$) introduced by a surface irregularity is calculated.

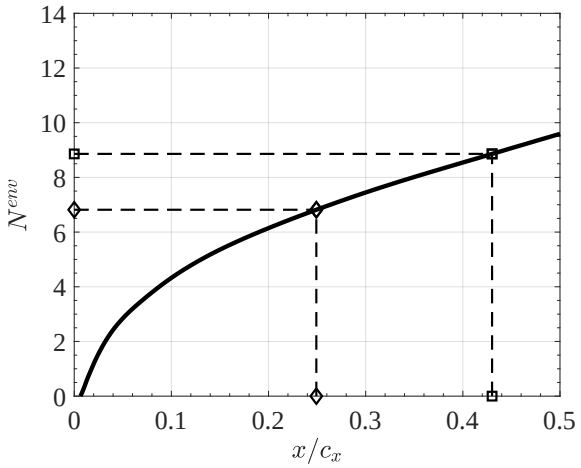

Fig. 10 Envelope of N-Factors curves (Clean-ST) for $\alpha = 2.9°$ and $Re_{c_X} = 2.95 \times 10^6$; □ →Clean-TR ($x_{t,C}/c_x = 0.43, N_C = 8.9$). ◊ →FFS-C ($x_{t,C}/c_x = 0.25, N_I = 6.8$).

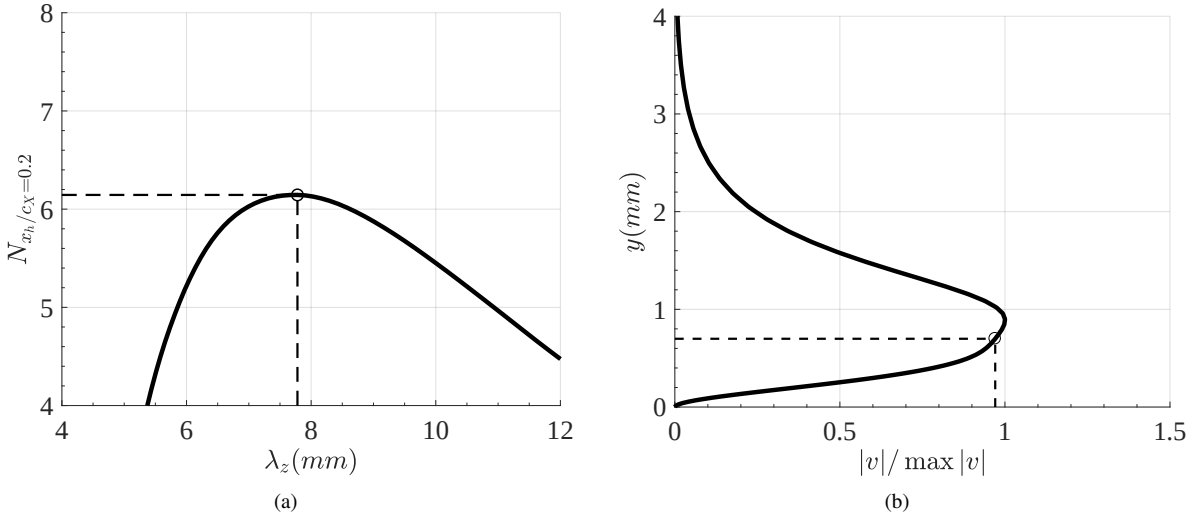

Fig. 11 Estimation of cross-flow instability vortices core height (y_c) from the Clean-ST case for $\alpha = 2.9°$ and $Re_{c_X} = 2.95 \times 10^6$; (a) N-factors of stationary cross-flow modes for different wavelengths (λ_z) at the step location ($x_{h_2}/c_x = 0.2$). (b) v-Perturbation mode shape corresponding to $\lambda_{z_{h_2}} = 7.78$ mm, with indication of the 97% maximum amplitude location and corresponding wall-normal height $y_c = 698$ μm

B. Cross-flow vortex core height estimation

Tufts et al. [14] proposed a physics-based criterion to determine the maximum allowable FFS height based on a numerical study of the interaction between the stationary cross-flow instability and the step surface irregularity.

The criterion is based on the observation that due to the inherent span-wise pressure gradient found in swept-wings, the recirculation region upstream and downstream of the FFS edge is not of two-dimensional nature. Rather, it is a helical flow with traveling direction from the root to tip for a backward-swept wing. Hence, they suggest that when the step height (h_2) is lower than the incoming cross-flow instability vortices (CFV's) core height (y_c) a destructive interaction occurs between the CFV's and the downstream helical flow. On the other hand, when the step height is higher ($h_2 > y_c$), a constructive interaction exist, resulting in a displacement of the transition front towards the step due to an amplification of stationary crossflow modes.

As outlined in [14], the CFV's core height (y_c) can be estimated from the results of an Orr-Sommerfeld linear stability analysis based on the clean case (i.e. smooth no surface irregularities). This is done by calculating the wall-normal height of the maximum amplitude of the v-perturbation eigenfunction, corresponding to the most amplified wavelength at the step location. Considering the LST calculations for the condition $\alpha = 2.9°$ at $Re_{c_X} = 2.95 \times 10^6$, envelope of N-Factors presented in Fig. 10. The wavelength of the most amplified stationary cross-flow instability mode is calculated by extracting the N-Factors of all the modes as a function of the span-wise wavelength (λ_z) at the location of the step and determining the maximum N-Factor. For this case, the most amplified stationary cross-flow mode at the step location ($x_{h_2}/c_X = 0.2$) results in a span-wise wavelength of $\lambda_{z_{h_2}} = 7.78$ mm as presented in Fig. 11(a).

From the corresponding v-perturbation eigenfunction for this wavelength, the height (y_c) is estimated by calculating the wall-normal height of 97% of the maximum amplitude of the mode shape as in [14]. For this case the estimated CFV's core height corresponds to $y_c = 698$ μm, as presented in Fig. 11(b).

IV. Results

The overall effect on the laminar-to-turbulent boundary layer transition, resulting from the addition of a forward facing step surface irregularity on a swept-wing, is described using IR measurements acquired and processed as detailed in Sec.II.D. An analysis is conducted where the transition behavior is determined from the change in transition front location and pattern for different FFS cases. Later, the change in the amplification factor ΔNcaused by the addition of the surface irregularities, is analyzed.

A. Transition Behavior

The location of the transition front was determined from the infrared thermographic measurements by processing the IR images for each experimental condition, as described in Sec. II.D. Figure.12 presents the change in the transition location (x_t/c_x) for increasing Re_{c_X} at a fixed angle of attack ($\alpha = 2.9°$) for the Clean-TR and the FFS - A,B and C cases.

For the Clean-TR case, an increase in Re_{c_X} leads to a gradual upstream movement of the transition front, starting from $x_{t,C}/c_x = 0.63$ at $Re_{c_X} = 2.13 \times 10^6$, up to a position upstream of the surface irregularity location (dashed-line in Fig. 12) $x_{t,C}/c_x = 0.18$ at $Re_{c_X} = 5.92 \times 10^6$.

The addition of $\bar{h}_2 = 951\mu$m forward facing step (FFS-C,see Table. 2) results in a distinct behavior with increasing Re_{c_X}, departing abruptly from the trend indicated by the Clean-TR case and reaching a position $x_{t,I}/c_x = 0.25$ at $Re_{c_X} = 2.95 \times 10^6$. Moreover, as evidenced by the confidence bounds of the linear fit used during the transition identification (error-bars in Fig.12), a jagged arrangement of turbulent wedges starting near the step and propagating downstream is observed. In contrast, adding a smaller step (FFS-B, $\bar{h}_2 = 734\mu$m, see Table. 2) initially results in a similar behavior as the Clean-TR case, showing a gradual change in the transition front location up until $Re_{c_X} = 2.75 \times 10^6$ from which then onwards the behavior changes and follows the one observed for the FFS-C case, reaching a location $x_{t,I}/c_x = 0.22$ at $Re_{c_X} = 4.01 \times 10^6$.

B. Critical Step Height

Based on the observed transition behavior (Sec. IV.A), for a fixed Re_{c_X} and α, three different regimes are identified. A subcritical one, in which the transition front pattern and location is nearly unaffected by the presence of the step. A critical one, in which the transition front pattern differs from the Clean-TR case and the transition location moves upstream towards the step location, abruptly departing from the trend indicated by the Clean-TR case. A supercritical in which transition occurs in the vicinity of the step.

Considering the experimental conditions $Re_{c_X} = 2.7 \times 10^6$ and $\alpha = 2.9°$ (Fig. 13), a supercritical condition is observed for the FFS-C configuration, causing an upstream displacement of the transition front to a lo-

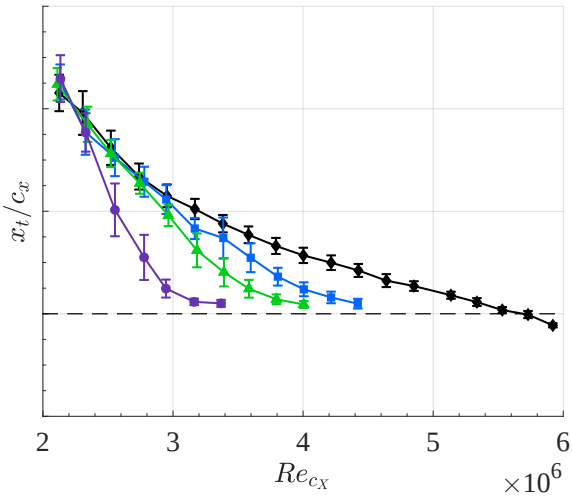

Fig. 12 Transition location for $\alpha = 2.9°$ at varying Re_{c_X}. Dashed black line indicates the surface irregularity chord-wise position $x_{h_2}/c_x = 0.2$; Clean-TR (♦), FFS-A (■), FFS-B (▲) and FFS-C (●).

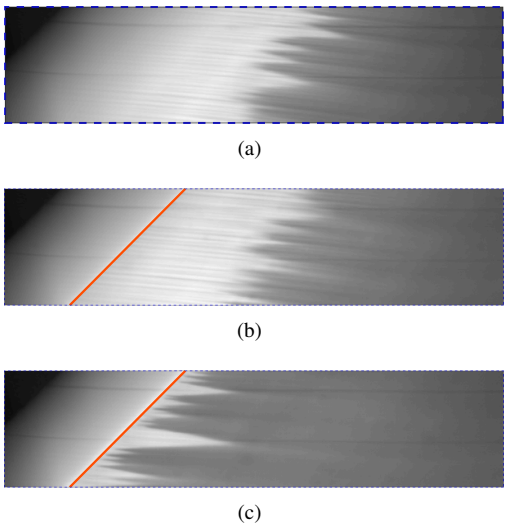

Fig. 13 Infrared thermography visualization (flow direction is from left to right) showing the effect of a 2D FFS surface irregularity at $x_{h_2}/c_x = 0.2$ on the transition location for $\alpha = 2.9°$ and $Re_{c_X} = 2.7 \times 10^6$; (a) Clean-TR. (b) FFS-B, $\bar{h}_2 = 734\mu$m. (c) FFS-C, $\bar{h}_2 = 951\mu$m

Table 3 Measured to critical step height ratio for $Re_{c_X} = 2.7 \times 10^6$ at $\alpha = 2.9°$

Criteria	FFS-B ($\bar{h}_2/h_c$)	FFS-C ($\bar{h}_2/h_c$)
Perraud et al [11]	1.21	1.57
Duncan et al [13]	0.93	1.21
Tufts et al [14]	0.99	1.29

cation in the vicinity of the step, Fig.13(c). On the other hand a subcritical behavior is observed for FFS-B, as the laminar-to-turbulent transition process appears to be unaffected by its presence (see Fig.13(b)).

From the literature available, it seems that no general agreement has been reached regarding the local or global parameters that should be used to estimate the FFS critical step height in a swept-boundary layer. Perraud et al[11] observed that the ratio between the step height and the local boundary layer displacement thickness provided a good indication. Duncan et al[13] presented an empirical fit based on experimental data and, recently, Tufts et al[14] presented a criterion based on the interaction between the CFV's and the recirculation region downstream of the FFS edge, shortly discussed in Sec. III.B.

For the configurations FFS-B and FFS-C, the ratio between the measured ($\bar{h}_2$) and the critical step height (h_c) was calculated for the condition $Re_{c_X} = 2.7 \times 10^6$ at $\alpha = 2.9°$ and presented in Table. 3. The critical ratio $h_2/\delta^*_{h_2} = 1.5$ observed in [11] for CFI dominated flow, leads to an under-prediction of the tolerable FFS step height, as a supercritical situation is estimated for the FFS-B case. The empirical fit presented in [13] seems better suited to this case, as it leads to a subcritical (FFS-B) and a supercritical (FFS-C) estimation. Finally, the criteria presented in [14] predicts a near critical condition for the FFS-B and a supercritical condition for the FFS-C. It is important to note that there is a difference among the definitions of the criterion. The definition presented in [13] considers as a critical step height, the one which will cause the movement of the transition location close or at the step. However, the definition presented in [14] is based on the step height that will significantly affect the transition process leading to a degradation of the laminar flow due to an amplification of stationary crossflow modes.

C. Transition Front Pattern

An analysis of the transition front pattern with respect to the ratio between the CFV's core height and step height (y_c/h_2) is presented in this section for the FFS-B configuration. This case changes between the subcritical, critical and supercritical regime in the range $2 \times 10^6 < Re_{c_X} < 4 \times 10^6$ at a fixed $\alpha = 2.9°$, as shown from the identified transition location presented in Fig. 12.

Figure. 14 displays a comparison of the transition front pattern, between the Clean-TR and the FFS-B configuration as captured in the IR measurements. As expected, the transition front displays a jagged arrangement of turbulent wedges, suggesting that stationary CFI is responsible for the laminar breakdown of the boundary layer flow.

For the Clean-TR case (left side of Fig. 14) an increase in Re_{c_X} results in a progressive movement of the front with a mild change in the transition front pattern. At $Re_{c_X} \approx 2.3 \times 10^6$,the FFS-B and the Clean-TR configuration display a very similar (almost identical) transition front pattern (Fig. 14(a) and 14(b)), clearly evidencing a subcritical situation ($y_c/\bar{h}_2 = 1.2$ and $\bar{h}_2/\delta^*_{h_2} = 1.59$, Fig. 15) where the addition of this surface irregularity appears to have a negligible effect on the laminar-to-turbulent boundary layer transition.

An increase in Re_{c_X}, does not produce an evident change in the transition front pattern until $Re_{c_X} = 2.97 \times 10^6$ (Fig. 14(h)), where the transition pattern presents a noticeable change when compared to the Clean-TR case (Fig. 14(g)). At this condition turbulent wedges appear closer to the step location suggesting that the effect of the step is no longer negligible. The analysis of the ratio between the estimated CFV's core height and the measured step height ($y_c/\bar{h}_2 = 0.95$, red circle in Fig. 15) indicates an undergoing critical situation. From this point onwards, the transition location rapidly departs from the trend indicated by Clean-TR (see Fig. 12) resulting in an upstream displacement of the transition front towards the FFS location.

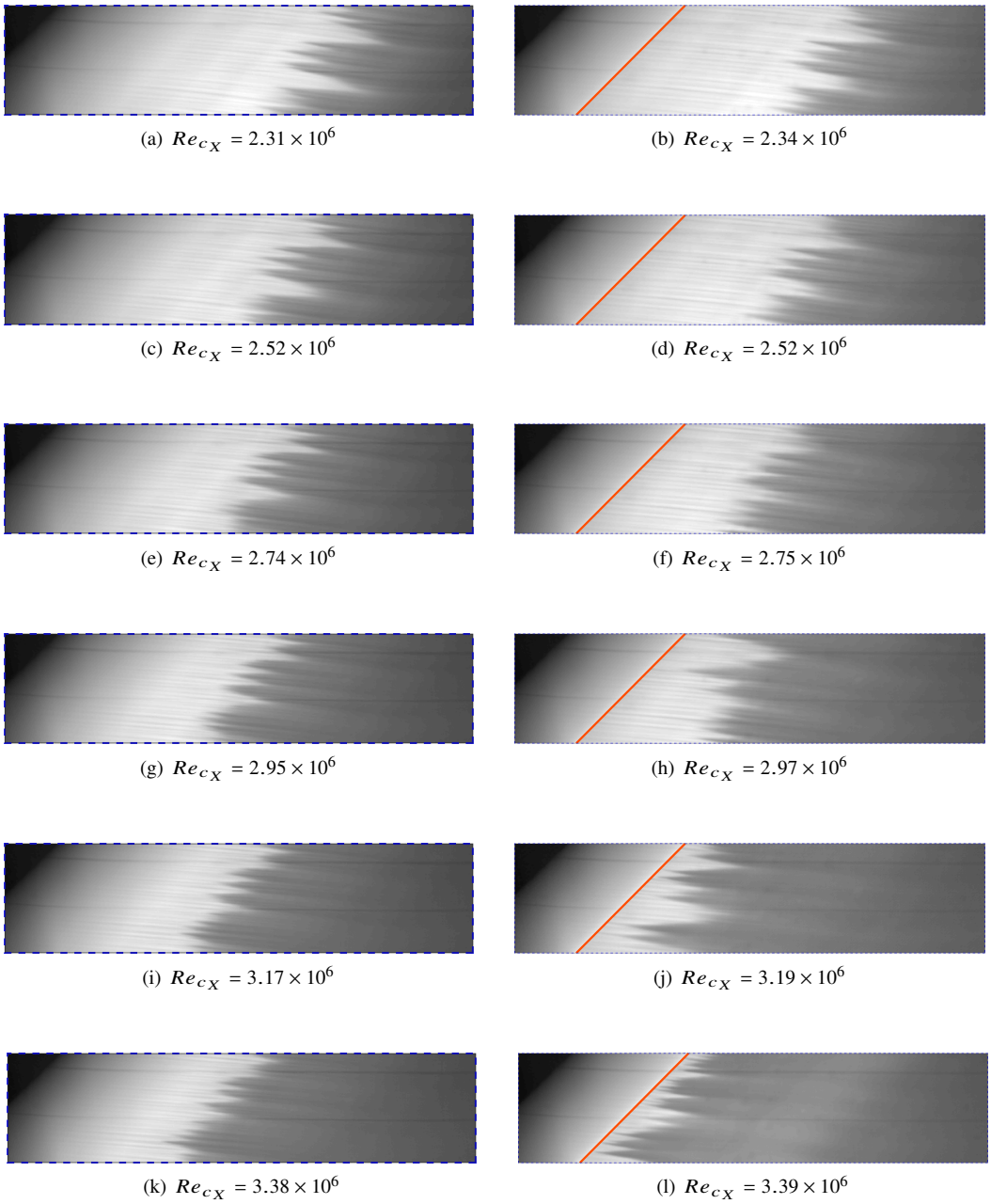

(a) $Re_{c_X} = 2.31 \times 10^6$ (b) $Re_{c_X} = 2.34 \times 10^6$

(c) $Re_{c_X} = 2.52 \times 10^6$ (d) $Re_{c_X} = 2.52 \times 10^6$

(e) $Re_{c_X} = 2.74 \times 10^6$ (f) $Re_{c_X} = 2.75 \times 10^6$

(g) $Re_{c_X} = 2.95 \times 10^6$ (h) $Re_{c_X} = 2.97 \times 10^6$

(i) $Re_{c_X} = 3.17 \times 10^6$ (j) $Re_{c_X} = 3.19 \times 10^6$

(k) $Re_{c_X} = 3.38 \times 10^6$ (l) $Re_{c_X} = 3.39 \times 10^6$

Fig. 14 Infrared thermography visualization (flow direction is from left to right) displaying the effect of a 2D FFS surface irregularity at $x_{h_2}/c_x = 0.2$ on the transition front pattern for $\alpha = 2.9°$ and varying Re_{c_X}; Left, Clean-TR case. Right, FFS-B case $\bar{h}_2 = 734\mu$m

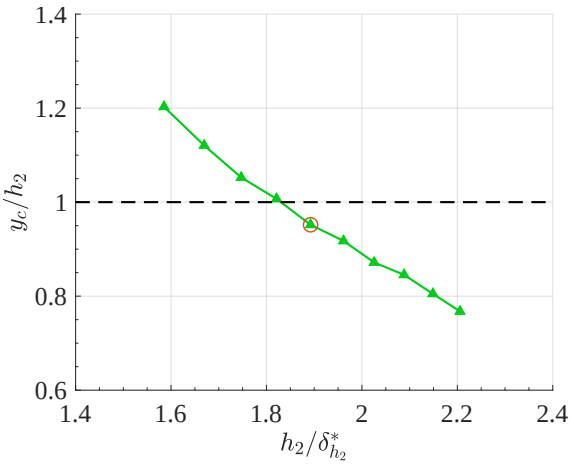

Fig. 15 Variation of estimated CFV's core height to measured step height ratio with decreasing boundary layer displacement thickness at a fixed step height (FFS-B, $\bar{h}_2 = 734\mu$m, see Table. 2).

D. ΔN results

The influence that a forward facing step has on the laminar-to-turbulent boundary layer transition is characterized by calculating the reduction (ΔN) in the critical N-factor induced by the addition of the step. This approach has been traditionally used in the study of surface irregularities for both TS and CFI dominated cases [5, 6, 11, 12].

Based on the IR measurements, for all the cases FFS-A, B, and C, the transition front location was identified as described in II.D, with an upstream limit set to 0.5% downstream of the step location, for the remaining combinations of α and Re_{c_X}. Later, a linear stability calculation (LST) was performed based on the Clean-ST pressure distribution to calculate the ΔN-factors, as described in Sec. III.A. Moreover, LST results for each condition were used to estimate the CFV's core height (y_c) following the procedure described in [14] and outlined in Sec. III.B.

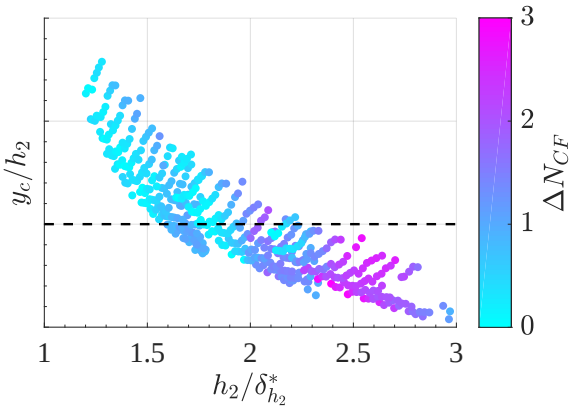

Fig. 16 Correlation between reduction of N-factor and a combination of step height relative to the estimated CFV's core height and boundary layer displacement thickness

The resulting ΔN-factors corresponding to different combinations of the ratio $h_2/\delta^*_{h_2}$ and y_c/h_2 are presented in Fig. 16. When analyzing these results, it is important to consider that an increase in Re_{c_X} results in a decrease in the boundary layer displacement thickness (δ^*) and a decrease in the estimated CFV's core height (y_c). A general agreement is observed regarding the critical ratio ($y_c/h_2 = 1$, dashed black line in Fig. 16), it is clear that when this ratio is $y_c/h_2 >> 1$, the addition of a FFS step will result in a negligible effect of the step in the boundary layer transition process, leading to a low or mild reduction in the N-factors. However, if the ratio is $y_c/h_2 << 1$, the transition process seems to be highly affected by the FFS resulting in a strong reduction of the N-factors. Moreover, these results suggest that the relative step height play an important role as an increase in the ratio $h_2/\delta^*_{h_2}$ leads to a stronger reduction in N-factors for the same y_c/h_2 ratio.

V. Conclusions

An experimental study was conducted to investigate the overall effect that surface irregularities in the form of forward facing steps, have in the laminar-to-turbulent boundary layer transition when dominated by stationary cross-flow instabilities. FFS add-ons were manufactured and installed on the surface of the M3J swept-wing model.

The results presented in this study show that infrared thermography is a powerful flow measurement technique capable of determining the overall transition behavior when performing large parametric studies. Moreover, when processing the IR images, a differential approach is suggested to reduce the background noise caused by the surface irregularity.

Upon the addition of a FFS, three distinct regimes are identified. A subcritical one, which leads to a negligible effect in the transition location and front pattern. A supercritical regime in which there was a noticeable change in the transition front pattern, and the transition location rapidly shifted upstream towards the step location, departing in this way from the trend indicated by the clean baseline. A supercritical regime in which transition occurs in the vicinity of the step. Moreover, it was observed that the limit between the subcritical and critical regime is in good agreement with the method proposed by Tufts et al[14] to estimate the FFS critical step height.

The reduction in the critical N-factor (ΔN) caused by the FFS, was calculated for three step heights cases at different combinations of Reynolds number and angle of attack conditions. A relation was found between the reduction of the critical N-factor, the estimated cross-flow vortex core height to step height ratio (y_c/h_2), and the relative step height ($h_2/\delta^*_{h_2}$). When the ratio $y_c/h_2 >> 1$, a mild reduction in the critical N-factor is observed. On the other hand, a ratio $y_c/h_2 << 1$ leads to a strong reduction in the critical N-factor. Additionally, the results show that an increase in the relative step height ratio ($h_2/\delta^*_{h_2}$) results in an higher critical N-factor reduction for a fixed y_c/h_2 ratio. This trends indicate the importance of considering both parameters in the determination of the effect of FFS step in the laminar-to-turbulent boundary layer transition when dominated by cross-flow instabilities.

The work presented in this paper is part of an ongoing research project to characterize the effect that surface irregularities have on boundary layer transition. The ΔN-method offers an overview of the phenomena related to FFS, capable of guiding future investigations into the underlying flow mechanisms and the role that the step geometry plays in it.

Acknowledgments

This research is conducted under the financial support of Embraer S.A. through the Laminar Flow Technology Project. The authors express their gratitude to J. Cavalcanti and G. Becker for their support during the wind tunnel campaigns and to Dr. Jacopo Serpieri for sharing his expertise in the study of cross-flow instability. To P. Duyndham, N. Van Beeck, L. Moelenwijck and S. Bernardy for sharing their technical knowledge during the experimental preparation and to the TUD Aerospace Material and Structures Laboratory for providing advice and equipment to manufacture and measure the surface irregularity add-ons. Finally, a special mention goes to Aerospace student J. Katamay for his contribution during these experiments.

References

[1] IATA, "IATA Forecasts Passenger Demand to Double Over 20 Years," Press release no.59, International Air Transport Association, 2016. [Online] Available: www.iata.org/pressroom/pr/Pages/2016-10-18-02.aspx [Accessed 10-Oct-2017].

[2] Macintosh, A., and Wallace, L., "International aviation emissions to 2025: Can emissions be stabilised without restricting demand?" *Energy Policy*, Vol. 37, No. 1, 2009, pp. 264–273. doi: 10.1016/j.enpol.2008.08.029.

[3] Thibert, J., Reneaux, J., and Schmitt, V., "ONERA activities on drag reduction," *17th Congress on International Council of the Aeronautical Sciences*, 1990, pp. 1053–1064.

[4] Skorupa, A., and Skorupa, M., *Riveted lap joints in aircraft fuselage: design, analysis and properties*, Springer Science & Business Media, 2012, Vol. 189, pp. 1–9. doi: 10.1007/978-94-007-4282-6.

[5] Wang, Y., and Gaster, M., "Effect of surface steps on boundary layer transition," *Experiments in Fluids*, Vol. 39, No. 4, 2005, pp. 679–686. doi: 10.1007/s00348-005-1011-7.

[6] Crouch, J., Kosorygin, V., and Ng, L., "Modeling the effects of steps on boundary-layer transition," *In: Govindarajan R. (eds) IUTAM Symposium on Laminar-Turbulent Transition. Fluid Mechanics and Its Applications*, Vol. 78, Springer, 2006, pp. 37–44. doi: 10.1007/1-4020-4159-4_4.

[7] Tani, I., "Effect of two-dimensional and isolated roughness on laminar flow," *In: Lachmann (ed.) Boundary layer and flow control*, Vol. 2, 1961, pp. 637–656.

[8] Holmes, B. J., Obara, C. J., Martin, G. L., and Domack, C. S., "Manufacturing tolerances for natural laminar flow airframe surfaces," Tech. rep., SAE Technical Paper, 1985. doi: 10.4271/850863.

[9] Drake, A., Bender, A. M., and Westphal, R. V., "Transition due to surface steps in the presence of favorable pressure gradients," *26th AIAA Applied Aerodynamics Conference*, AIAA Paper 2008-7334, 2008. doi: 10.2514/6.2008-7334.

[10] Costantini, M., Risius, S., and Klein, C., "Experimental investigation of the effect of forward-facing steps on boundary layer transition," *Procedia IUTAM*, Vol. 14, 2015, pp. 152–162. doi: 10.1016/j.piutam.2015.03.036.

[11] Perraud, J., and Seraudie, A., "Effects of steps and gaps on 2D and 3D transition," *European Congress on Comp. Methods in Applied Science and Eng., ECCOMAS*, 2000.

[12] Perraud, J., Arnal, D., and Kuehn, W., "Laminar-turbulent transition prediction in the presence of surface imperfections," *International Journal of Engineering Systems Modelling and Simulation 48*, Vol. 6, No. 3-4, 2014, pp. 162–170. doi: 10.1504/IJESMS.2014.063129.

[13] Duncan, G. T., Crawford, B. K., Tufts, M. W., Saric, W. S., and Reed, H. L., "Effects of step excrescences on a swept wing in a low-disturbance wind tunnel," *52nd Aerospace Sciences Meeting*, AIAA Paper 2014-0910, 2014. doi: 10.2514/6.2014-0910.

[14] Tufts, M. W., Reed, H. L., Crawford, B. K., Duncan, G. T., and Saric, W. S., "Computational investigation of step excrescence sensitivity in a swept-wing boundary layer," *AIAA Journal of Aircraft*, Vol. 54, No. 2, 2016, pp. 602–626. doi: 10.2514/1.C033892.

[15] Saeed, T. I., Mughal, M. S., and Morrison, J., "The Interaction of a Swept-Wing Boundary Layer with Surface Excrescences," *54th AIAA Aerospace Sciences Meeting*, AIAA Paper 2016-2065, 2016. doi: 10.2514/6.2016-2065.

[16] Beguet, S., Perraud, J., Forte, M., and Brazier, J.-P., "Modeling of Transverse Gaps Effects on Boundary-Layer Transition," *AIAA Journal of Aircraft*, Vol. 54, No. 2, 2017, pp. 794–801. doi: 10.2514/1.C033647.

[17] Eppink, J. L., "Stereo Particle Image Velocimetry Measurements of Transition Downstream of a Foward-Facing Step in a Swept-Wing Boundary Layer," *55th AIAA Aerospace Sciences Meeting*, AIAA Paper 2017-0306, 2017. doi: 10.2514/6.2017-0306.

[18] Eppink, J. L., "The Effect of Forward-Facing Steps on Stationary Crossflow Instability Growth and Breakdown," *2018 AIAA Aerospace Sciences Meeting*, AIAA Paper 2018-0817, 2018. doi: 10.2514/6.2018-0817.

[19] Serpieri, J., and Kotsonis, M., "Design of a swept wing wind tunnel model for study of cross-flow instability," *33rd AIAA Applied Aerodynamics Conference*, AIAA Paper 2015-2576, 2015. doi: 10.2514/6.2015-2576.

[20] Serpieri, J., and Kotsonis, M., "Three-dimensional organisation of primary and secondary crossflow instability," *Journal of Fluid Mechanics*, Vol. 799, 2016, pp. 200–245. doi: 10.1017/jfm.2016.379.

[21] Serpieri, J., Yadala Venkata, S., and Kotsonis, M., "Conditioning of cross-flow instability modes using dielectric barrier discharge plasma actuators," *Journal of Fluid Mechanics*, Vol. 833, 2017, pp. 164–205. doi: 10.1017/jfm.2017.707.

[22] Yadala, S., Hehner, M. T., Serpieri, J., Benard, N., Dörr, P. C., Kloker, M. J., and Kotsonis, M., "Experimental control of swept-wing transition through base-flow modification by plasma actuators," *Journal of Fluid Mechanics*, Vol. 844, 2018. doi: 10.1017/jfm.2018.268.

[23] Serpieri, J., "Cross-Flow Instability Flow diagnostics and control of swept wing boundary layers." Ph.D. thesis, Delft University of Technology, 3 2018. Pp.28-29, doi: 10.4233/uuid:3dac1e78-fcc3-437f-9579-048b74439f55.

[24] Raffel, M., and Merz, C. B., "Differential infrared thermography for unsteady boundary-layer transition measurements," *AIAA Journal*, Vol. 52, No. 9, 2014, pp. 2090–2093. doi: 10.2514/1.J053235.

[25] Raffel, M., Merz, C. B., Schwermer, T., and Richter, K., "Differential infrared thermography for boundary layer transition detection on pitching rotor blade models," *Experiments in Fluids*, Vol. 56, No. 2, 2015, p. 30. doi: 10.1007/s00348-015-1905-y.

[26] Haralick, R. M., and Shapiro, L. G., *Computer and robot vision*, Addison-Wesley Longman Publishing Co., Inc., 1992, Vol. 1, pp. 28–48.

[27] Otsu, N., "A threshold selection method from gray-level histograms," *IEEE transactions on systems, man, and cybernetics*, Vol. 9, No. 1, 1979, pp. 62–66.

[28] Schlichting, H., and Gersten, K., *Boundary-layer theory*, Cambridge University Press, 2000.

[29] Arnal, D., "Boundary layer transition: predictions based on linear theory," *In AGARD, Special Course on Progress in Transition Modelling 63 p (See N94-33884 10-34)*, 1993.

Errata

- In section V. Conclusions, the third sentence of the third paragraph should read: "A **critical** regime in which there was a noticeable change in the transition front pattern, and the transition location rapidly shifted upstream towards the step location, departing in this way from the trend indicated by the clean baseline."